PAPER

The effect of nanorod position on the plasmonic properties of the complex nanorod in nanohole arrays

To cite this article: Yanfeng Wang et al 2021 J. Phys. D: Appl. Phys. 54 155201

View the <u>article online</u> for updates and enhancements.



IOP ebooks™

Bringing together innovative digital publishing with leading authors from the global scientific community.

Start exploring the collection-download the first chapter of every title for free.

J. Phys. D: Appl. Phys. 54 (2021) 155201 (8pp)

https://doi.org/10.1088/1361-6463/abd80f

The effect of nanorod position on the plasmonic properties of the complex nanorod in nanohole arrays

Yanfeng Wang¹, Zhengjun Zhang^{2,*} and Yiping Zhao^{1,2,*}

E-mail: zjzhang@tsinghua.edu.cn and zhaoy@uga.edu

Received 24 October 2020, revised 17 December 2020 Accepted for publication 4 January 2021 Published 29 January 2021



Abstract

By moving the nanorod (NR) from the middle toward the rim of the nanohole (NH), i.e. breaking the geometric symmetry, the extraordinary optical transmission (EOT) caused by the dipole coupling of the localized surface plasmon resonance of the NR and the NH can be tuned to redshift exponentially while maintaining the high transmission and overall dimension of the structural unit. This resonant wavelength shift depends strongly on the moving direction of the NR, i.e. whether it is along the long axis or short axis of the rod. Connecting the NR to the NH and increasing the lattice period can significantly redshift the EOT mode, allowing ultra-high transmission in the mid-infrared (MIR) region. The high local E-fields, enhanced propagating waves with a tunable visible-MIR resonance wavelength, make this structure suitable for the design of compact and integrated optical devices from the visible to the MIR wavelength range. In addition, Fano resonances are emerging due to the coupling and hybridization of different plasmonic modes, making the structure beneficial for high sensitivity measurement.

Supplementary material for this article is available online

Keywords: mid-infrared transmission, extraordinary optical transmission, nanorod array, nanohole array, tunable transmission, Fano resonance

(Some figures may appear in colour only in the online journal)

1. Introduction

Metasurfaces have revolutionized the field of optics by enabling wavefront engineering and manipulating light-matter interactions. Among the various metasurface structures studied, the complex subwavelength nanohole (NH) arrays, i.e. NHs combined with other nanostructure arrays, such as hole-particle [1–3], hole-disk [2–4], rod on hole [5], rod in hole [2, 6–9] and split hole structures [8, 10–12], have recently become the focus of research due to their peculiar extraordinary optical transmission (EOT) properties.

The combination of the hole and other nanostructures offers more parametric design freedom, and new optical phenomena can be realized. In particular, the nanorod (NR) in NH arrays shows unique polarization-dependent optical properties [13–16], demonstrates optical nonlinearity [17, 18], and Fano resonance [4, 15, 19] that involves the discrete state of oscillating systems coupled to continuum states. Our recent studies show that a new EOT mode emerges when the Ag NH in a hexagonal array is combined with an NR in the middle [5, 9, 16, 20]. This new EOT mode, caused by the coupling of the localized surface plasmon resonance (LSPR) of the NR and NH, appears at a longer wavelength with respect to that of the normal EOT mode, redshifts exponentially with the NR length, induces high transmission, generates

© 2021 IOP Publishing Ltd Printed in the UK

¹ Key Laboratory of Advanced Materials (MOE), School of Materials Science and Engineering, Tsinghua University, Beijing 100084, People's Republic of China

² Department of Physics and Astronomy, University of Georgia, Athens, GA 30602, United States of

^{*} Authors to whom any correspondence should be addressed.

strong near-field enhancements, and exhibits epsilon-nearzero properties. The extremely small size, ultra-compact structure arrays, and the ability to achieve enhanced transmission in the visible to near-infrared (NIR) region make this NR in NH (NRinNH) structure very suitable for the design of tunable NIR optical devices [17], and a good index sensor [16] and surface enhanced spectroscopy sensor [20]. However, in [9], the adjustable wavelength region of the EOT is limited up to the NIR region by the length of the NRs for a fixed NH diameter and array periodicity. Whereas the midinfrared (MIR) region is a technologically important spectral range, EOT in the MIR region has important research value in fields such as communication, sensing, and security applications [21, 22]. The development of tunable MIR plasmonic devices is especially attractive for a number of these applications [23]. However, much of the work in the field of EOT has focused on the visible, NIR, and terahertz regimes [24]. Thus, it is significant to further extend the adjustable spectral region of the new EOT mode of the NRinNH structures to the MIR band.

On the other hand, in the systematic study in [9], the NR is always positioned in the center of the NH, which possesses a high degree of symmetry. Other studies also show that if the NR is moved away from the center, i.e. connected to one side of the NH, the new EOT mode is also observed in the optical transmission spectra, but has a different resonance wavelength and transmission [5, 8, 16], which indicates that the position of the NR inside the NH should play an important role in determining its plasmonic properties. In fact, when a fixed-length NR is moving to a different location inside the NH, two effects are expected: the symmetry of the entire structure will be broken, which may induce Fano resonances; and the gaps between the two ends of the NR and the rim of the NH will vary, which suggests different near-field coupling effects between the NR and the NH. In studies of plasmonic coupling in noble metal nanostructures [25, 26], the near-field coupling between the noble metal nanoparticles results in the near-exponential redshift of the LSPR with the reduction in the inter-particle gap. Thus, reducing the gap between the NH and the NR may be helpful in further shifting the EOT mode of the NRinNH structures to the MIR region.

Inspired by plasmon near-field coupling, in the current work, the NR is moved to a closer position to the rim of the NH, and the geometric symmetry of NRinNH structures is broken. As a result, the new EOT mode of the Ag NRinNH structures can be tuned to redshift exponentially with the decrease in the gap distance between the NR and the rim of the NH. The breaking of the structural symmetry allows a wider adjustable spectral region of the EOT mode while maintaining the high transmission and overall dimension of the structure unit at the same time. We have systematically investigated how the position of the NR inside the NH, or the symmetry and coupling, affect the plasmonic properties of the NRinNH structures. We find that the redshift depends on the moving direction of the NR, which intrinsically depends on local electromagnetic (EM) field coupling between the NR and the NH. In addition, connecting the NR to the NH and increasing the lattice periodicity can induce a large redshift of the EOT mode, allowing ultrahigh transmission in the MIR region. The asymmetric combination of the NR and NH also induces the emergence of 'dark' higher-order plasmon resonances in the visible region under normal incidence, and Fano-like dips are created due to the destructive interference of the higher-order resonances with the overlapping EOT peak [27, 28]. The excitation of Fano resonances on EOT peaks can help improve the figure of merit of the spectral features and the sensitivity due to the changes in the refractive index (RI), which is beneficial for high sensitivity detection, including RI sensors [29], biosensors, and optical modulators.

2. FDTD calculations

2.1. Change rod position

Figure 1 shows how the position of a NR changes inside a NH. When a NR is moving along the x-axis, the reflection symmetry about the x-axis remains, and the gap $g_t(g_b)$ between the top (bottom) end of the NR and the rim of the NH is the same, i.e. $g_x = g_t = g_b$. When the NR is moving up along the y-axis, the mirror symmetry about the y-axis is maintained, but $g_t < g_b$. The NRinNH structure is a hexagonal array with a period of L, as shown in figure S1 (available online at stacks.iop.org/JPD/54/155201/mmedia). A commercial finite-difference-time-domain (FDTD) software system (Ansys Lumerical 2020 R2 Finite Difference IDE) was used to calculate the transmission spectra $T(\lambda, \varphi)$ and localized E_7 -field distributions of the asymmetric NRinNH structures. Here, the angle φ is defined between the polarization direction of the incident light and the long axis of NRs. A rectangular unit cell (the yellow box in figure S1 of the supporting information (SI)) was used with periodic boundary conditions in the x- and y-directions, and perfectly matched layer boundary conditions were used on the top and bottom surfaces of the calculation domain. The entire structure was immersed in a vacuum. The layer thickness (h), the hole diameter (D), the periodicity of the hexagonal lattice (L), the NR length (l), and width (w) were fixed to be 50 nm, 340 nm, 500 nm, 250 nm, and 30 nm, respectively, unless otherwise specified. In all calculations, a mesh size of $2 \text{ nm} \times 2 \text{ nm} \times 2 \text{ nm}$ was chosen, and the dielectric function of the Ag was taken from Johnson et al [30] The detailed FDTD conditions can be found in section S1 of the SI.

Some representative $T(\lambda,0^\circ)$ spectra of the NRinNHs when the NR is moving along the x- and y-axis are shown in figures 1(b) and (d). The $T_{\rm NH}(\lambda)$ spectrum of the pure NH array with the same lattice arrangement and dimension is also plotted as a reference (black dashed curve). In general, the $T_{\rm NH}(\lambda)$ spectra possess two EOT peaks (P_1 and P_2) caused by the surface plasmon resonance at the Ag-air and Ag-glass interfaces and two Wood's anomaly dips (D_1 and D_2), which are well characterized in the EOT community [31, 32]. For the NRinNHs, the $T(\lambda,0^\circ)$ has an additional peak P_3 around $\lambda=1.3-2.2~\mu{\rm m}$, which represents the new EOT mode induced by the dipole coupling of the LSPR of the NR and

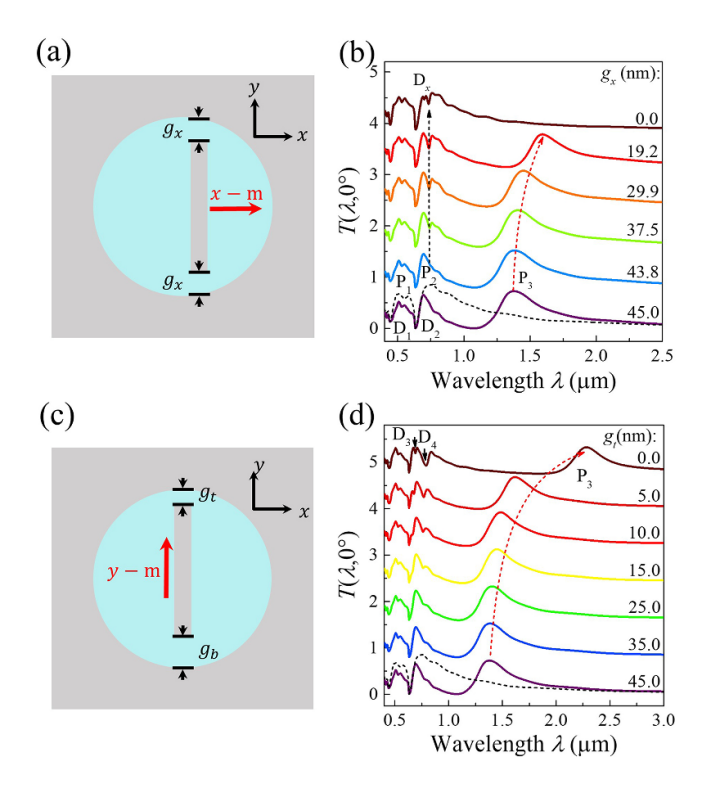


Figure 1. A schematic diagram of the plane of the asymmetric NRinNH array. The configuration of the asymmetric NRinNH array used in the FDTD calculations is shown in figure S1. The NR in the center of the NH is moved (a) horizontally along the *x*-axis (x - m) or (c) vertically along the *y*-axis (y - m) to form an asymmetric NRinNH array. The gap distances between the NR and the NH along the *y*-axis are termed as g_t and g_b , respectively. For x - m, $g_x = g_t = g_b$; for y - m, $g_t < g_b$. (b) The x - m and (d) y - m dependent $T(\lambda, 0^\circ)$ of NRinNH with D = 340 nm, L = 500 nm, l = 250 nm, and w = 30 nm.

NH based on the discussions in [9] and [16]. More specifically, when the NR is in the middle of the NH ($g_x = 45.0$ nm, the purple curve in figure 1(b)), the $T(\lambda_{P1}, 0^{\circ})$ in the corresponding P_1 and P_2 wavelength regions decreases and P_2 slightly blueshifts ($\lambda_{P2} = 695$) when compared to that of the pure NH, while the D_1 and D_2 dips remain unchanged. This demonstrates that the P_1 and P_2 peaks and the D_1 and D_2 dips in $T(\lambda,0^{\circ})$ of the NRinNHs have the same physical origins as those in $T_{NH}(\lambda)$. As the gap g_x decreases in x-m, the extra EOT peak P_3 redshifts with well-maintained high transmission, i.e. $T(\lambda_{P3}, 0^{\circ}) \sim 70.4\%$. Note that in figure 1(b), the case when the right corners of the NR are in contact with the NH (figure S2) is not included. Both the case where the NH and NR are completely separated ($g_x \le 19.2 \text{ nm}$) and the case when the entire ends of the NR are in contact with the NH ($g_x = 0$ nm) are considered. When $g_x = 0$ nm, the peak P_3 vanishes due to the 'disappearance' of the coupling effect between the NR and NH, as shown in figure 1(b). The dip D_x is observed on top of P_2 when $g_x < 40.0$ nm. The E_z -field distributions shown in figure S3 indicate that the resonance at λ_{Dx} is a dipole–quadrupole antibonding mode of the NR and NH. It has been theoretically predicted that the higherorder resonances of a metal nanoring can be excited at normal incidence through asymmetric coupling with a nanodisk [33, 34]. The excitation of higher-order modes is rationalized in terms of plasmon hybridization [35, 36]. The possible plasmon coupling diagram resulting in the dip D_x is proposed in figure 2(a), showing the origins of the dipole/multipole bonding and antibonding modes of the NRinNH structures [37, 38]. In figure 2(a), the in-phase dipolar plasmon coupling along the long axis of the NR contributes to the lowest energy resonance P_3 , while D_x is caused by the antibonding mode of the hybridization of the dipolar mode of the NR and quadrupole mode of the NH, where the dipolar mode of the NR and quadrupole mode of the NH are out-of-phase. When a narrow line-shape multipolar resonance spectrally overlaps with a broad dipolar resonance, the Fano-like interferences will be excited [28]. As the resonance position of the dipole-quadrupole antibonding mode is right on top of the super-radiant surface plasmon polariton (SPP) mode P_2 , the Fano-like dip D_x is the result of the interference between the dipole-quadrupole mode of the NH and NR and the SPP mode P_2 of the compound NH array [4]. The other hybridization modes in figure 2(a) that are not observed in the spectra are probably damped by the Wood's anomaly. A detailed discussion about D_x can be found in section S3 of the SI.

When the rod is moving along the y-axis, as shown in figures 1(c) and (d), as g_t decreases from 45.0 nm to 0.0 nm, two small dips, D_3 and D_4 , are observed successively on top of P_2 , and λ_{P3} redshifts from 1380 nm to 2280 nm. At $g_t < 20.0$ nm, dip D_4 first appears, and gradually redshifts with decreased transmission as g_t decreases. At $g_t < 15.0$ nm, another dip D_3 appears, and also shows a slight redshift trend with further decrease in g_t . The appearance of these two dips is due to the broken symmetry of the NRinNH structure along the polarization direction. The local E_z -field distributions at $\lambda_{\rm D3}$ and $\lambda_{\rm D4}$ of $g_{\rm t}=5.0$ and 0.0 nm are plotted in figure S4 to demonstrate the origins of the two dips. Based on the E_z -field distributions in figure S4, a possible plasmon coupling diagram is proposed in figure 2(b). The dip D_3 results from the overlap between the dipolar antibonding mode of the NH and NR, and the SPP P_2 of the complex NH array; while D_4 occurs with the interference between the dipole-quadrupole bonding mode of the NR and NH, and P_2 . Both the out-of-phase dipolar coupling and the quadrupole dipole plasmon coupling contribute to the higher-energy resonance band, while the in-phase dipolar plasmon coupling produces a relatively lower-energy resonance band for the bonding mode (P_3) , as shown in figure 2(b). A detailed discussion about the origins of D_3 and D_4 can be found in section S3 of the SI. The incident angle dependent properties of the dips were also studied and plotted in section S4 of the SI. When $\theta > 10^{\circ}$, λ_{D4} increases almost linearly with θ .

In addition to the two dips, the redshift of λ_{P3} shows a smaller magnitude when compared to that of the x-m with the same decrease in g_t , i.e. for $g_t = 25.0$ nm, $\lambda_{P3} \approx 1.493 \ \mu m$ for x-m, while $\lambda_{P3} \approx 1.40 \ \mu m$ for y-m. To better understand the redshift of λ_{P3} due to the change of NR position, λ_{P3} versus g_x and g_t relationships for NR moving along the x-axis and the y-axis are plotted together in figure 3. As demonstrated in [9] and figure 2, P_3 is attributed

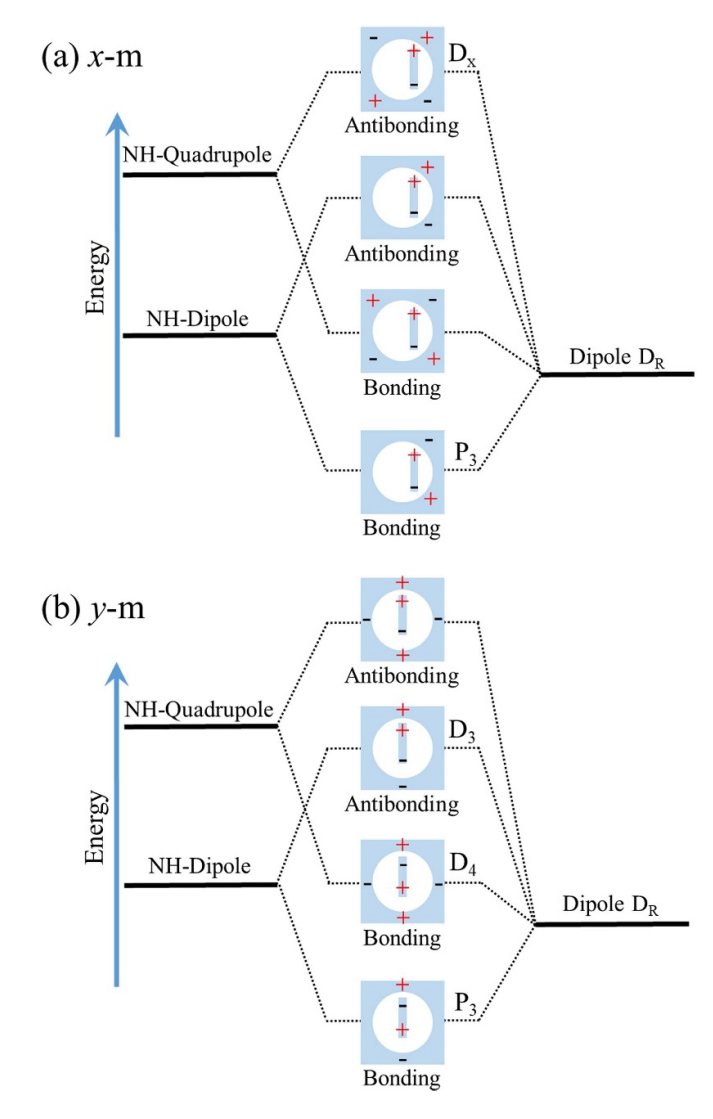


Figure 2. The proposed plasmon coupling diagram for (a) x-m and (b) y-m of the NRinNH structure derived from the FDTD calculations.

to the dipole coupling of the LSPR of the NR and NH. Based on the classical electrodynamics model, the plasmonic near-field coupling can be well described by a plasmon ruler equation: an exponential function or a power law [37–39]. The λ_{P3} versus g_x can be well fitted by an exponential function, $\lambda_{P3} = 1.357 + 1.24 \times e^{-\frac{8x}{11.5}}$ (the red dashed line in figure 3(a)), which verifies the conclusion in [9]. However, the trend of λ_{P3} versus g_t fits well to a linear superposition of two exponential functions, $\lambda_{P3} = 1.368 + 0.66 \times e^{-\frac{g_t}{2.4}} + 0.25 \times e^{-\frac{g_t}{12}}$ for $0.0 \leqslant g_t \leqslant 45.0$ nm and $\lambda_{P3} = 1.368 + 0.66 \times e^{-\frac{g_t}{2.4}} + 0.25 \times e^{-\frac{g_t-g_t}{12}}$ for $45.0 \leqslant g_t \leqslant 90.0$ nm (the black dashed line in figure 3(a)). This is because when the NR moves along the y-axis, there are two different gap configurations between the NR and the NH, which generates a strong EM coupling for the smaller gap and a weak EM coupling for the larger gap at the same time. Although the effect of the weak coupling is not significant, it still affects the redshift of λ_{P3} . Thus, the above fitting function reflects the joint effect of the two coupled gaps. When the NR moves along the x-axis, the two gaps are the same size, $g_x = g_t = g_b$. The coupling between the NH and NR of the two gaps is the same, thus λ_{P3} versus g_x can be fitted by a single exponential function. This can also explain that with the same g_t , the λ_{P3} of the x-m is larger than that of the y-m, i.e. for x-m, $g_b = g_t$, the coupling strengths in two gaps between the NR and the NH are the same; while for y-m, $g_b < g_t$, a weaker coupling at g_b is excepted.

The different EM coupling effect of the two different gaps of the y-m can also be visualized when the maximum $|E_{\text{max}}/E_0|^2$ and average local field $\langle |E/E_0|^2 \rangle$ of the two gaps are plotted as a function of g_t . As shown in figure 3(b), the $|E_{\text{max}}/E_0|^2$ and $\langle |E/E_0|^2 \rangle$ for the top gap increase monotonically from 859 and 218 to 11774 and 3107, respectively, when g_t decreases from 45.0 nm to 5.0 nm; while the $|E_{\text{max}}/E_0|^2$ and $\langle |E/E_0|^2 \rangle$ of the bottom gap decrease a little when g_t decreases from 45.0 nm to 25.0 nm. This is due to the fact that the increased gap distance (from 45.0 nm to 65.0 nm) for the bottom gap weakens the coupling between the NR and the NH. But when g_t decreases further, the $|E_{\text{max}}/E_0|^2$ and $\langle |E/E_0|^2 \rangle$ of g_b increased with the decrease of g_t . This is caused by two competing effects: one is the increased gap distance of g_b, which will weaken the coupling between the NR and the NH and cause the $|E_{\text{max}}/E_0|^2$ and $\langle |E/E_0|^2 \rangle$ to decrease. The other is the increased charge density at the end of the NR and the inside circumference of the NH at g_b due to the increased charge density at g_t , which will enhance the coupling between the NR and the NH and cause the $|E_{\text{max}}/E_0|^2$ and $\langle |E/E_0|^2 \rangle$ to increase. When g_t is smaller than 25.0 nm, the second effect dominates. The increased coupling strength between the NR and the NH at g_t leads to an increased charge density at the end of the NR (the inside circumference of the NH), which further caused the increased charge density at the other end of the NR (the other inside circumference of the NH) and caused the $|E_{\text{max}}/E_0|^2$ and $\langle |E/E_0|^2 \rangle$ to increase. The local E_z -field distributions of asymmetric NRinNH structures at λ_{P3} with different gt for y-m were compared in figure S6 to help understand the increased $|E_{\text{max}}/E_0|^2$ and $\langle |E/E_0|^2 \rangle$ of g_b when g_t decreased. Unlike the case when the NR is in the middle of the NH, of which the dipole bonding mode of the NR and NH at λ_{P3} is centrally symmetric (figures S6(a)–(c)), when the NR is moved toward the NH, the Coulomb attraction between the NR and NH at the gap g_t becomes stronger and stronger, drives the opposite charges on the NH to accumulate to locations near the end of the NR, and results in an increased local charge density and an asymmetrical charge distribution of the dipole mode. For the E_z -field distributions at λ_{P3} when $g_t = 5.0$ nm (figures S6(d)-(f)), a stronger field at the end of the NR (the inside circumference of the NH) at both the gaps g_t and g_b can be seen when compared to that of $g_t = 45.0$ nm, which means a higher charge density at $g_t = 5.0$ nm. Thus, the $|E_{\text{max}}/E_0|^2$ and $\langle |E/E_0|^2 \rangle$ at g_b will increase. When the NR finally connected to the NH ($g_t = 0.0$ nm, figures S6(g)–(i)), the surface charges at the connected end are allowed to be dissipated to the entire connected metal network, and the resonance at λ_{P3} changed to a strong out-of-plane dipole mode of the NR, which coupled with the in-phase out-of-plane dipole resonance of the rim of

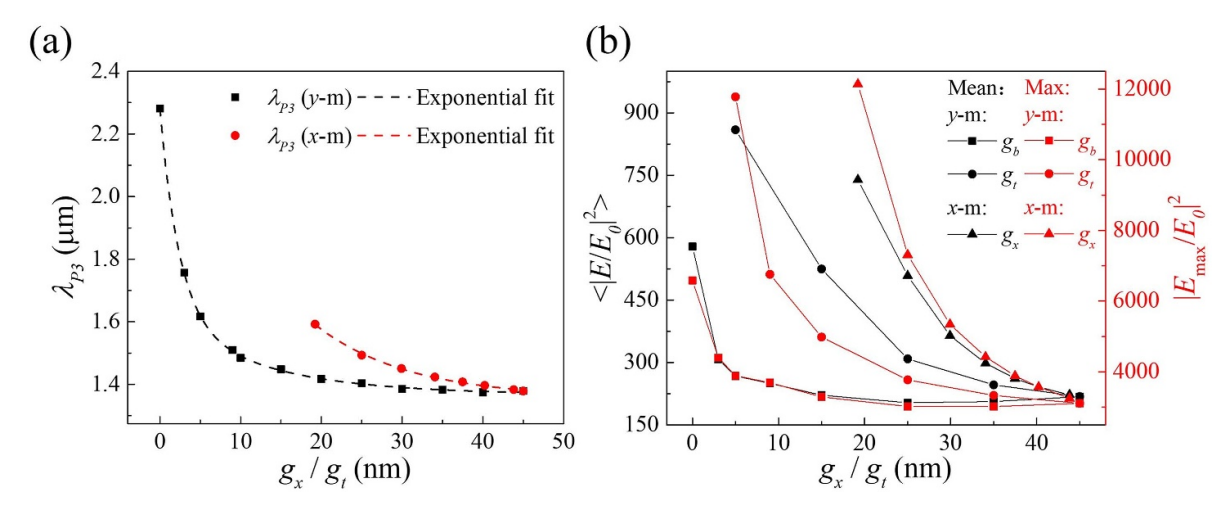


Figure 3. (a) The plot of λ_{P3} versus g_x and g_t for the NR moving along the *x*-axis and *y*-axis. (b) The plots of the volume maximum and average $|E/E_0|^2$ at λ_{P3} versus g_t and g_x .

the NH. The redistribution of the charges when g_t decreases, lowers the coupling energy and explains the redshift of λ_{P3} . Details can be found in section S5 of the SI.

The influence of x-m on the $|E_{\rm max}/E_0|^2$ and $<|E/E_0|^2>$ of the gaps has also been investigated and is plotted as a function of g_x in figure 3(b). The local E_z -field distributions of $g_x=25.0$ nm for x-m are shown in figure S7. The $|E_{\rm max}/E_0|^2$ ($<|E/E_0|^2>$) of g_x increases monotonically from 3250 (222) to 12 136 (739) when g_x decreases from 45.0 nm to around 19.2 nm. Due to the joint effect of the coupling of the NR and the NH in the two same-sized gaps, the field enhancement of g_x is much higher than that of the y-m with the same-sized g_t . For example, for $g_t=25.0$ nm in y-m ($g_b=70.0$ nm), the maximum and average $|E/E_0|^2$ in g_t are 315 and 3775; while for $g_x=g_t=25.0$ nm in x-m, the maximum and average $|E/E_0|^2$ are 508 and 7308 in g_t , which are almost double the corresponding values.

2.2. Change rod length

Since the λ_{P3} redshifts significantly when the NR is connected to the NH at y-m, it would be interesting to see how the EOT mode P_3 changes with the length l of the NR when the NR is connected to the NH (con-NRinNH). Figure 4(a) shows a $T(\lambda, 0^{\circ})$ map when l is varied from 10 nm to 350 nm. When *l* increases from 30 nm to 335 nm, λ_{P3} can be shifted from 778 nm to around 3700 nm, which covers the largest wavelength range of the NIR region. This is very significant for such a small plasmonic structure to tune the resonance in such a large wavelength region. Besides D_3 and D_4 , discussed above in figure 1(d), some other small Fano-like dips due to the excitation of higher-order modes are also observed (details in figure S8 in section S6 of the SI). The wavelength, as well as transmission, of all the resonances are plotted in figure S9. The peak P_3 begins to show when l > 30 nm in length (figure S10) and keeps redshifting with the increase in l. Figure 4(b) plots $\lambda_{\rm P3}$ and $T(\lambda_{\rm P3},0^{\circ})$ of both con-NRinNH and when the NR is in the center of the NH (cen-NRinNH structure) versus different l. $T(\lambda_{P3}, 0^{\circ})$ of the con-NRinNH is about 0.2 lower than that of the cen-NRinNH with the same l, but comparing λ_{P3} of the con-NRinNH to that of the cen-NRinNH, to achieve the same resonance wavelength, e.g. 2280 nm for l = 250 nm of the con-NRinNH, *l* needs to be around 327 nm for the cen-NRinNH. In other words, the effective rod length for the con-NRinNH is much longer than litself. For the con-NRinNH structure, when l falls between 0 and 300 nm, the shifting trend of λ_{P3} versus l follows a power function: $\lambda_{P3} = 0.70 + 0.0015 \times l^{1.26}$, and in this region, $T(\lambda_{P3}, 0^{\circ})$ decreases slowly with the increase in l. A further increase in *l* beyond 300 nm gives rise to a significant shift in λ_{P3} , and $T(\lambda_{P3}, 0^{\circ})$ decreases rapidly. The redshift of λ_{P3} in this rod length region fits well to an exponential function, $\lambda_{P3}=2.69+1.06\times 10^{-11}\times e^{0.076\cdot l}$. This implies that around 300 nm a critical l exists, at which the gap between the NR and NH at the disconnected end is small enough that strong EM coupling between the NR and NH would take place and thus have a significant influence on the transmission of the con-NRinNH structure [7]. The critical l when strong EM coupling occurs for the cen-NRinNH is also around 300 nm. The fitting function at the two different rod length regions of the cen-NRinNH structure are $\lambda_{P3} = 0.79 + 7 \times 10^{-7} \times l^{2.5}$, and $\lambda_{P3} = 1.67 + 8.13 \times 10^{-15} \times e^{0.098 \cdot l}$. When l = 340 nm, which means the two ends of the NR are all connected on the NH and no coupling between the NR and NH exists, P_3 disappears for both the con-NRinNH and cen-NRinNH structures due to the release of the accumulated charges, to the entire metal network.

The strong coupling effect of the con-NRinNH when l > 300 nm can also be observed when the $|E_{\rm max}/E_0|^2$ and $<|E/E_0|^2>$ of the gap between the NR and NH are plotted as a function of l, as shown in figure 4(c) (the field enhancement of the cen-NRinNH is also plotted as a reference). Generally, the enhanced field increases with l, and both the $|E_{\rm max}/E_0|^2$ and $<|E/E_0|^2>$ of the con-NRinNH are stronger than those of the cen-NRinNH with the same l. The behavior of the enhanced fields versus l for both the con-NRinNH and cen-NRinNH follow similar trends to $\lambda_{\rm P3}$ or $T_{\rm P3}$ versus l, which is due to

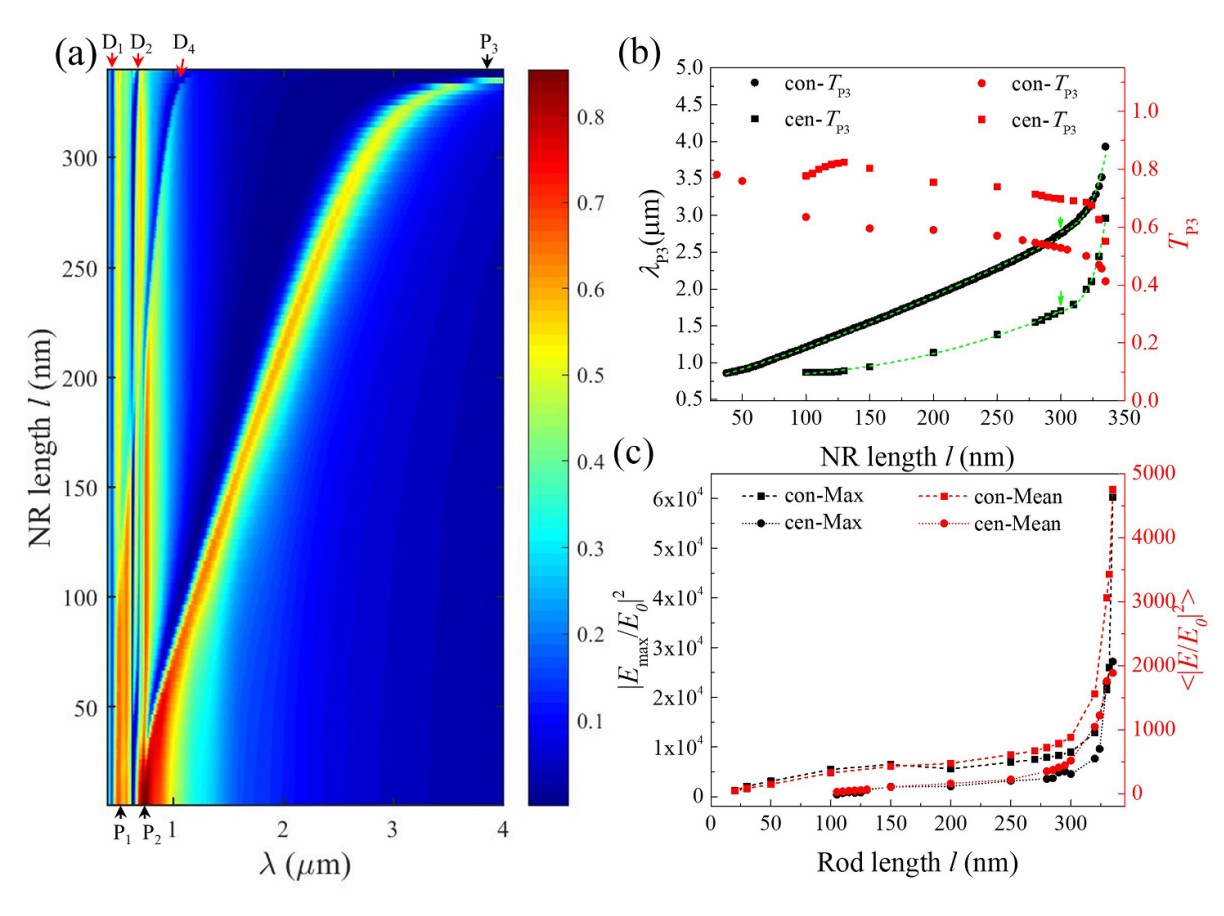


Figure 4. (a) The FDTD calculated $T(\lambda, 0^{\circ})$ of the con-NRinNH with different l. (b) The plot of λ_{P3} and $T(\lambda_{P3}, 0^{\circ})$ of the con-NRinNH and cen-NRinNH versus l. The green dashed curves are the fitting results. (c) The volume maximum and average $|E/E_0|^2$ at λ_{P3} versus l for the con-NRinNH and cen-NRinNH.

the change in the EM coupling strength in the gap. When l falls between 0 and at the critical l, both $|E_{\rm max}/E_0|^2$ and $<|E/E_0|^2>$ increase almost linearly but slowly with l. When l is larger than the critical l, the field enhancement rises sharply (the $<|E/E_0|^2>$ rises from around 880 to around 4700 and the $|E_{\rm max}/E_0|^2$ sharply rises from 8960 to around 60 000 when l increases from 300 nm to 334 nm for the con-NRinNH, while for the cen-NRinNH, the $<|E/E_0|^2>$ rises from around 520 to around 1880 and the $|E_{\rm max}/E_0|^2$ sharply rises from 4550 to around 27 200 when l increases from 300 nm to 334 nm).

2.3. Change lattice periodicity

Figure 4(b) shows that with a slight change in the NR length l, the spectral range of $\lambda_{\rm P3}$ can be tuned significantly, from $\sim 0.8~\mu \rm m$ to $\sim 3.7~\mu \rm m$. Such a property is very important for the design of plasmonic-based optical components and devices. In addition, based on the understanding of the EOT properties of the pure NH structures, the period L of the lattice is another factor that could be used to tune the spectral response of plasmonic properties. It is expected that the L could also have a significant effect on tuning the $\lambda_{\rm P3}$. Figure 5(a) shows the L dependent $T(\lambda,0^\circ)$ spectra of the con-NRinNH structures for fixed D/L, l/L and w/L ratios ($D=0.88\times L$, $l=0.86\times L$)

L and $w = 0.10 \times L$). Since the calculations will cover the MIR response, the substrate for the FDTD calculations was changed to polyimide (the dielectric constant is 2.67), which is transparent in the infrared and terahertz range. As shown in figure 5(a), both λ_{P2} and λ_{P3} redshift linearly with L (P_1 is not well distinguishable from figure 5(a)). To better illustrate the tunable wavelength region of λ_{P3} of the asymmetric NRinNH structures, λ_{P3} with different rod position (figure 1), different l (figure 4), and different L (figure 5(a)) are plotted together in figure 5(b), while the T_{P3} $(T(\lambda_{P3}, 0^{\circ}))$ with different rod position (figure 1), different l (figure 4), and different L (figure 5(a)) are plotted in figure 5(c). When L increases from 0.5 μ m to 2.0 μ m, as shown in figure 5(b), $\lambda_{\rm P3}$ redshifts linearly from \sim 6 $\mu{\rm m}$ to \sim 20 $\mu{\rm m}$. The slopes of λ_{P2} and λ_{P3} versus L are determined to be 2.82 and 9.31, respectively, which means λ_{P3} was much more sensitive to the change in L than λ_{P2} , i.e. the effect of L on λ_{P3} is more significant. In addition, during the change in the lattice period L, the transmission peak T_{P3} remains almost a constant, with a relatively high transmission >0.55 (figure 5(c)). Thus, overall, figure 5(b) shows that for the NRinNH structures, the y-m moving and l change causes λ_{P3} to be tuned continuously from the visible to the NIR and the L change enables λ_{P3} be tuned to the MIR with a well-maintained high transmission.

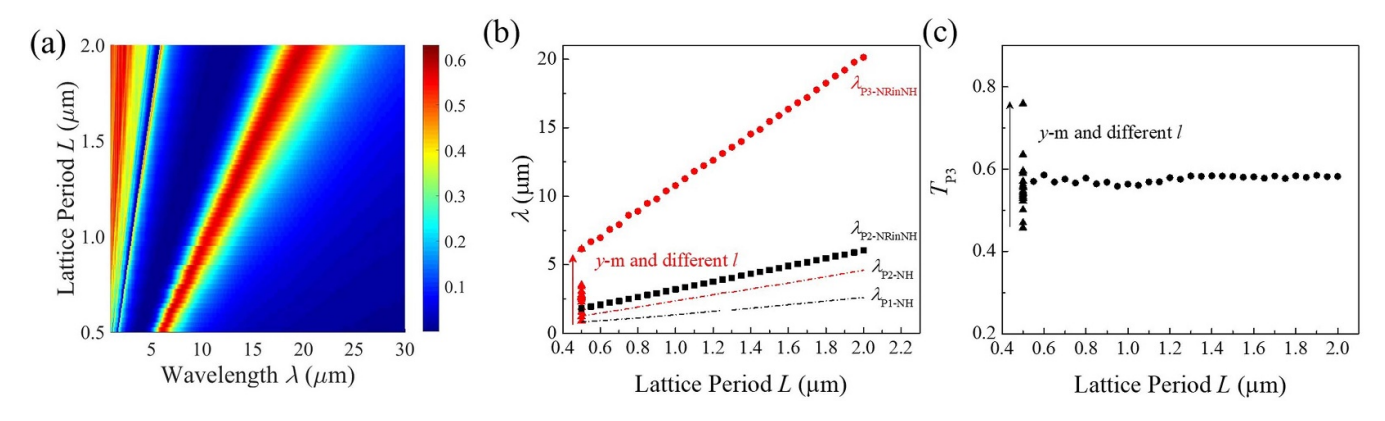


Figure 5. (a) The FDTD calculated $T(\lambda,0^\circ)$ of the con-NRinNH with different L ($D=0.88\times L$, $l=0.86\times L$ and $w=0.10\times L$). (b) The plot of λ_{P2} and λ_{P3} (dotted plots) of asymmetric NRinNH, and λ_{P1} and λ_{P2} (dash-dotted lines) of NH versus L. (c) The plot of $T(\lambda_{P3},0^\circ)$ of asymmetric NRinNH versus L.

On the other hand, with the increase in L, the λ_{P1} and λ_{P2} for the pure NH structures also redshift linearly according to the following equation [40]:

$$\lambda_{\rm P1} = \frac{\sqrt{3}L}{2} \sqrt{\frac{\varepsilon_{\rm m}}{\varepsilon_{\rm m} + 1}}, \lambda_{\rm P2} = \frac{\sqrt{3}L}{2} \sqrt{\frac{\varepsilon_{\rm m}\varepsilon_{\rm glass}}{\varepsilon_{\rm m} + \varepsilon_{\rm glass}}}. \quad (1)$$

As shown in figure 5(b), the slopes of λ_{P1} and λ_{P2} versus L for the pure NH structures are determined to be 1.21 and 2.22, respectively, which are much smaller than that (9.31) of λ_{P3} versus L for the con-NRinNH structures with the same D/L ratio. Thus, to achieve an EOT peak at the same targeted wavelength region, the pure NH structures should have a much larger L than that of the NRinNH structures. For example, to realize an EOT peak (P2) at $\lambda_{P2}\sim 20~\mu m$ (corresponding to $\lambda_{P3} = 20.14 \ \mu \text{m}$ of the con-NRinNH structure for $L = 2.0 \ \mu \text{m}$ and $l = 1.72 \mu m$), L needs to be around 16 μm for a pure NH array, i.e. the unit cell size of the NH structures would be eight times larger than that of the con-NRinNH structure. In the meantime, with this D/L ratio ($D = 0.88 \times L$), the two normal EOT peaks (P_1 and P_2) for the pure NH structures were rather weak; only a very broad spectrum with a low transmission in the MIR could be observed (section S7 of SI). And even with an increase in L, no EOT peak can be observed in the MIR region. Thus, the fine tunability and ultra-high transmission in the MIR region of P_3 make the NRinNH structure a more favorable choice for compact and integrated optics and optical devices.

3. Conclusions

In conclusion, we have systematically investigated how the position of the NR inside the NH affects the plasmonic properties of the complex NRinNH structures. We demonstrate that with the decrease in the gap distance between the NR and the inside circumference of the NH, the resonance wavelength of the new EOT mode redshifts exponentially. Different redshift patterns of the new EOT mode are observed when the

NR is moved along its long axis and short axis. The broken structural symmetry enables the excitation of the quadrupole LSPR mode of the NH under normal incidence and brings interesting plasmon resonances into effect that otherwise are not possible. In addition, the asymmetry coupling allows the new EOT mode (P_3) to have a broader adjustable resonance wavelength range, maintains a high transmission, and keeps the overall dimension of the structural unit almost the same. Specifically, the y-m moving causes the new EOT mode to be tuned continuously from visible to NIR. If the length of the NR and the lattice periodicity are further increased ($D = 0.88 \times$ $L, l = 0.86 \times L$ and $w = 0.10 \times L$, L changes from 0.5 μ m to $2.0 \mu m$) for the con-NRinNH structure, the new EOT mode can be tuned from 0.5 μ m to the MIR region (>20 μ m). Such a result demonstrates that one can use a very small feature-sized structure to tune a large wavelength spectroscopic response: for example, using a sub-visible wavelength structure to tune an infrared response, or a micro-sized structure to tune an MIR or even a far-infrared response. Therefore, from a technological point of view, the conventional nanolithography and microfabrication process can be used to create similar complex plasmonic structures that cover the spectroscopy response in the entire EM wavelength region. Experimentally, to realize the systematical change in the NR position in an NH array, both electron beam lithography or focused ion-beam lithography are the techniques of choice. But the overall areas fabricated by these two methods are small, which requires spectroscopic microscopy to characterize the optical properties. However, large area NRinNH structures can also be achieved on infrared transparent substrates using a shadowing nanosphere lithography developed recently by us [16].

Acknowledgments

YFW and ZJZ were financially supported by the Basic Science Centre Project of NSFC under Grant No. 51788104 and the Chinese National Natural Science Foundation (Grant No.

51761145045). YPZ was financially supported by the National Science Foundation under Grant No. ECCS-1808271.

ORCID iDs

Yanfeng Wang https://orcid.org/0000-0001-7698-6230 Zhengjun Zhang https://orcid.org/0000-0001-8727-6373 Yiping Zhao https://orcid.org/0000-0002-3710-4159

References

- [1] Wei H, Hakanson U, Yang Z, Hook F and Xu H 2008 Small 4 1296–300
- [2] Wu S, Wang Q J, Yin X G, Li J Q, Zhu D, Liu S Q and Zhu Y Y 2008 Appl. Phys. Lett. 93 101113
- [3] Du B, Yang Y, Zhang Y, Jia P, Ebendorff-Heidepriem H, Ruan Y and Yang D 2019 J. Phys. D: Appl. Phys. 52,275201
- [4] Li L, Liang Y, Peng W and Liu Y 2018 Opt. Mater. Express 8 2131-9
- [5] Larson S, Luong H, Song C and Zhao Y 2019 J. Phys. Chem. C 123 5634–41
- [6] Li J, Cushing S K, Zheng P, Meng F, Chu D and Wu N 2013 Nat. Commun. 4 2651
- [7] Wang C et al 2010 Appl. Phys. Lett. 96 251102
- [8] Li Z-B, Zhou W Y, Kong X-T and Tian J-G 2010 *Opt. Express* **18** 5854–60
- [9] Wang Y, Luong H, Zhang Z and Zhao Y 2020 J. Appl. Phys. 53 275202
- [10] Li Z-B, Zhou W Y, Kong X-T and Tian J-G 2010 *Plasmonics* **6** 149–54
- [11] Balykin V I and Melentiev P N 2018 Phys.-Usp. 61 133-56
- [12] Melentiev P N, Afanasiev A E, Kuzin A A, Gusev V M,
 Kompanets O N, Esenaliev R O and Balykin V I 2016 *Nano*Lett. 16 1138–42
- [13] Huang W X, Wang Q J, Yin X G, Huang C P, Huang H, Wang Y M and Zhu Y Y 2011 *J. Appl. Phys.* **109** 114310
- [14] He M D, Liu J Q and Wang K J 2012 *J. Phys. D: Appl. Phys.* **45** 345304
- [15] Zhang F, Huang X, Zhao Q, Chen L, Wang Y, Li Q, He X, Li C and Chen K 2014 Appl. Phys. Lett. 105 172901
- [16] Wang Y, Chong H B, Zhang Z and Zhao Y 2020 ACS Appl. Mater. Interfaces 12 37435–43
- [17] Abb M, Wang Y, Papasimakis N, Groot C H D and Muskens O L 2014 Nano Lett. 14 346–52

- [18] Melentiev P N, Afanasiev A E, Kuzin A A, Baturin A S and Balykin V I 2013 Opt. Lett. 38 2274–6
- [19] Luk'yanchuk B, Zheludev N I, Maier S A, Halas N J, Nordlander P, Giessen H and Chong C T 2010 Nat. Mater. 9 707–15
- [20] Song C, Jiang X, Yang Y, Zhang J, Larson S, Zhao Y and Wang L 2020 ACS Appl. Mater. Interfaces 12 31242–54
- [21] Li S Q, Guo P, Zhang L, Zhou W, Odom T W, Seideman T, Ketterson J B and Chang R P H 2011 ACS Nano 5 9161–70
- [22] Passmore B S, Allen D G, Vangala S R, Goodhue W D, Wasserman D and Shaner E A 2009 Opt. Express 17 10223
- [23] Anglin K, Ribaudo T, Adams D C, Qian X, Goodhue W D, Dooley S, Shaner E A and Wasserman D 2011 J. Appl. Phys. 109 123103
- [24] Banerjee S, Lok Abhishikth N, Karmakar S, Kumar D, Rane S, Goel S, Azad A K and Roy Chowdhury D 2020 J. Opt. 22 125101
- [25] Jain P K and El-Sayed M A 2010 Chem. Phys. Lett. 487 153–64
- [26] Huang F and Baumberg J J 2010 Nano Lett. 10 1787–92
- [27] Hao F, Nordlander P, Sonnefraud Y, Dorpe P V and Maier S A 2009 ACS Nano 3 643–52
- [28] Habteyes T G, Dhuey S, Cabrini S, Schuck P J and Leone S R 2011 Nano Lett. 11 1819–25
- [29] Karmakar S, Kumar D, Varshney R K and Chowdhury D R 2020 J. Appl. Phys. 53 415101
- [30] Williams M L 1996 Occup. Environ. Med. 53 504-504
- [31] Wood R W 1935 Phys. Rev. 48 928-36
- [32] Rodrigo S G 2012 Extraordinary optical transmission *Optical Properties of Nanostructured Metallic Systems* (Berlin:

 Springer) pp 37–75
- [33] Hao F, Sonnefraud Y, Dorpe P V, Maier S A, Halas N J and Nordlander P 2008 *Nano Lett.* **8** 3983–8
- [34] Fu Y H, Zhang J B, Yu Y F and Luk'yanchuk B 2012 ACS Nano 6 5130-7
- [35] Yang D J, Yang Z J, Li Y Y, Zhou L, Hao Z H and Wang Q Q 2014 *Plasmonics* 10 263–9
- [36] Zhao K, Huo Y, Liu T, Li J, He B, Zhao T, Liu L and Li Y 2015 *Plasmonics* **10** 1041–8
- [37] Jain P K, Huang W and El-Sayed M A 2007 *Nano Lett.* **7** 2080–8
- [38] Aćimović S S, Kreuzer M P, González M U and Quidant R 2009 ACS Nano 3 1231–7
- [39] Cha H, Yoon J H and Yoon S 2004 ACS Nano 8 8554-63
- [40] Li Y 2017 Plasmonic Optics: Theory and Applications
 Tutorial texts in optical engineering; volume TT 110
 (Bellingham, WA: SPIE Press)